Soft Matter

PAPER

View Article Online
View Journal | View Issue

Cite this: *Soft Matter*, 2025, **21**, 4467

Control of monolayer sheet size and spatial order in colloidal assemblies by drying sessile drops of suspensions on oil layers

Santosh Vasant Daware,[abcd] Amelia C. Y. Liu,[b] Ranganathan Prabhakar *[c] and Guruswamy Kumaraswamy *[a]

Received 1st March 2025,
Accepted 5th May 2025

DOI: 10.1039/d5sm00215j

rsc.li/soft-matter-journal

We investigate the assembly of monodisperse polymer-coated polystyrene colloids during the evaporation of sessile drops on oil-coated substrates. In our system, the particles rapidly adsorb at the air–water interface, and as evaporation proceeds, those left behind in the shrinking droplet, are immediately captured by the moving interface. In sufficiently dilute dispersions, nearly all particles adsorb well before the interface becomes saturated, leading to the formation of monolayer sheets. In contrast, at higher particle concentrations, the interface saturates while a significant fraction of particles remain in the bulk, preventing monolayer formation. At any particle concentration, the thickness of the oil layer relative to the initial drop size plays a key role in determining whether monolayers form. The thinnest oil layers provide the broadest range of particle concentrations for successful monolayer assembly. A minimal theoretical model, based on rapid adsorption and negligible influence of internal flows, predicts the boundary between monolayer and non-monolayer regimes with good agreement to experiment. This suggests that interface saturation–not capillary flow–is the controlling mechanism in these drop-on-oil systems. Finally, analysis of the hexatic order parameter reveals that crystalline domain size increases with particle number. These findings offer a pathway to tune monolayer structure and order through controlled drying protocols, with potential applications in 2D materials and functional coatings.

1 Introduction

Understanding colloidal assembly driven by sessile droplet evaporation has important implications for inkjet printing, functional coatings, pesticide spraying, microfluidics, and diagnostics.[1,2] These applications demand precise control over deposit patterns and scalable long-range order to enhance performance. For instance, in inkjet printing, reproducible control over droplet deposition is essential for fabricating high-resolution functional devices.[1] Similarly, in photonic crystal fabrication, uniform nanoparticle deposition is crucial for achieving the desired optical properties.[3] Evaporation-driven assembly also enables the formation of hierarchical colloidal patterns, governed by factors such as temperature gradients, evaporation rates, and the properties of solutes, solvents, and substrates.[4]

Research on evaporation-driven colloidal assembly was sparked by the seminal work of Deegan *et al.* (1997),[5] which explained the coffee-ring effect. When a sessile droplet containing colloidal particles evaporates on a solid substrate, the evaporative flux varies across the liquid–air interface. For small droplets, surface tension causes the liquid interface to adopt a spherical cap shape. This geometric constraint, combined with mass conservation, induces an internal flow: as the droplet loses volume due to evaporation, liquid within the droplet redistributes to maintain its shape, resulting in internal fluid motion. Since suspended particles typically do not adsorb at the interface, they are advected by the internal flow as the liquid evaporates. On substrates where the contact line remains pinned, this flow transports particles to the contact line, forming the characteristic coffee-ring pattern. This basic process can be controlled by various strategies to modify the characteristics of the deposit. For instance, adding surfactants induce Marangoni flows that counteract the base internal flow leading to a uniform deposition on the substrate, rather than a ring at the contact line.[6] Another method to realize homogeneous drying patterns is to add high molecular-weight surface-active polymers that coat the particle surfaces and facilitate particle adsorption at the water–air interface.[7]

[a] *Department of Chemical Engineering, Indian Institute of Bombay, Mumbai, 400076, India. E-mail: guruswamy@iitb.ac.in*
[b] *School of Physics and Astronomy, Monash University, Clayton, 3800, Australia*
[c] *Department of Mechanical and Aerospace Engineering, Monash University, Clayton, 3800, Australia. E-mail: prabhakar.ranganathan@monash.edu*
[d] *IITB-Monash Research Academy, Indian Institute of Bombay, Mumbai 400076, India*

These observations raise the fascinating possibility of exploiting the liquid–air interface as a platform for 2D colloidal assemblies. In a previous work,[8] we demonstrated the formation of colloidal monolayers by drying sessile droplets containing colloids and polyethylenimine (PEI) on an oil-coated substrate. Crosslinking the PEI linked the colloids in the monolayer. We could control the size of these monolayers and the crystalline order of the particles by varying the droplet volume and particle concentration. By doping the suspension with small amounts of differently-sized particles, we were able to induce defects in the crystalline domains and selective dissolution of these particles controllably produced holes in the monolayers. We demonstrated the ability to resuspend the monolayers into other fluids and to transfer them to other substrates to allow them to be easily imaged using optical microscopy. This versatility makes these colloidal assemblies attractive as model systems for fundamental studies as colloidal analogues of 2D-materials. For instance, we used optical microscopy and image analysis to probe the influence of crosslinking on the flexibility of the monolayers.

The formation of colloidal monolayers in our system suggests a mechanism distinct from the conventional coffee-ring effect, where particles accumulate at the pinned contact line due to evaporative flows. Instead, the presence of an oil layer appears to play a critical role in regulating particle adsorption at the liquid–air interface, leading to the formation of well-defined monolayers. This raises important questions: how does the oil layer influence the availability of the interface for particle adsorption? What determines whether the particles form a disordered or crystalline monolayer, and how do particle concentration and oil-layer thickness govern this transition? Here, we systematically investigate these questions, identifying the conditions under which ordered or disordered monolayers emerge. We have previously demonstrated a method for fabricating polymerized colloidal monolayers by evaporating particle-laden drops on a silicone-oil layer of fixed thickness.[8] That study characterized the resulting monolayers in terms of their size, flexibility, and particle ordering, and highlighted the critical role of the underlying oil layer in successful monolayer formation. In the present work, we build upon these findings by systematically examining how the oil layer thickness affects the dynamics of colloidal particle assembly at the air–water interface. In particular, we provide an explanation for our observation that monolayers fail to form when the initial particle concentration exceeds a critical value, which depends on the oil layer thickness. We also investigate how the oil layer thickness influences the spatial ordering of particles in the final monolayer. Our findings provide new insight into how oil-mediated interfacial assembly can be harnessed to control the structure and properties of colloidal monolayers, with implications for designing functional 2D colloidal materials.

2 Materials

Monodisperse PS latex (1.08 ± 0.02 μm) were obtained from Microparticles GmbH, Germany as 10% w/v dispersions. These particles carry a negative surface charge due to the presence of sulphonic acid groups. PEI (branched, M_w = 25 000 g mol^{-1}), hexadecyltrimethoxysilane (HDTMS, purity ≥ 85%), poly(ethylene glycol) diglycidyl ether (PEGDE, M_n = 500 g mol^{-1}), and silicone oil (50 cSt) were procured from Sigma-Aldrich and used as received. All experiments were conducted using Milli-Q water (pH = 7, resistivity = 18.2 MΩ cm) obtained from a Millipore system.

3 Methods

3.1 Preparation of oil-coated glass substrates

Square glass coverslips (Blue Star; 22 mm side and thickness 0.16 mm) were cleaned by sonication with isopropyl alcohol for 15 minutes. The glass substrates were hydrophobized as described earlier.[8] Briefly, clean glass slides were placed in a methanol solution containing 2% HDTMS and sonicated for 30 minutes. These surface modified glass slides were washed extensively with isopropyl alcohol and then air dried. A water drop placed on a hydrophobised glass slide shows a contact angle of 98.2 ± 3.6°. Thin oil layers (<35 μm) were achieved by spin coating the silane-treated glass slide with silicone oil (50 cSt). Oil layers thicker than 35 μm were obtained by placing the coverslip in a Petri dish filled with the required quantity of silicone oil. The volume of silicone oil needed is calculated by subtracting the volume occupied by the coverslip from the total volume of the desired oil layer, which includes both the height of the coverslip and the required thickness of the oil. The silicone oil spread easily over the hydrophobized coverslip, and the petridishes were kept undisturbed for 30 min to allow uniform spreading of oil layer. Drop drying experiments were performed on the coverslip placed within the Petri dish and covered with oil.

Oil layer thickness was measured by calibrating the microscope travel, at first focusing on the coverslip and then on the oil layer surface. We adhere 1 μm colloids to the coverslip surface before adding the silicone oil and focus on these using the microscope fine adjustment knob. We performed measurements at various locations on coated substrates and this typically gave us thickness values that were within ±1 μm. The maximum sample-to-sample variability (across 3–4 coated coverslips) ranged from 10.8 μm for a film thickness of 95 μm; 7.8 μm for 48 μm films; 4.9 μm for 35 μm films and 2.6 μm for 10 μm films. For thin oil layers prepared by spin coating, we were able to weigh the samples and estimate the oil film thickness (since the area of the cover slip and the density of the silicone oil are known). This independent gravimetric estimate of the oil film thickness was in good accord with the measurement using the optical microscope.

3.2 Drying experiments

PS particle suspensions containing PEI were prepared as described earlier (Fig. 1A).[8] A 1 μL aliquot of PS latex suspension (~10^9 particles) was diluted in 100 μL Milli-Q water, and sonicated for 2 min, and further vortexed for 2 min to obtain a uniform colloidal dispersion. A PEI stock solution was prepared by dissolving 1 mg of PEI in 10 mL of Milli-Q water, and a

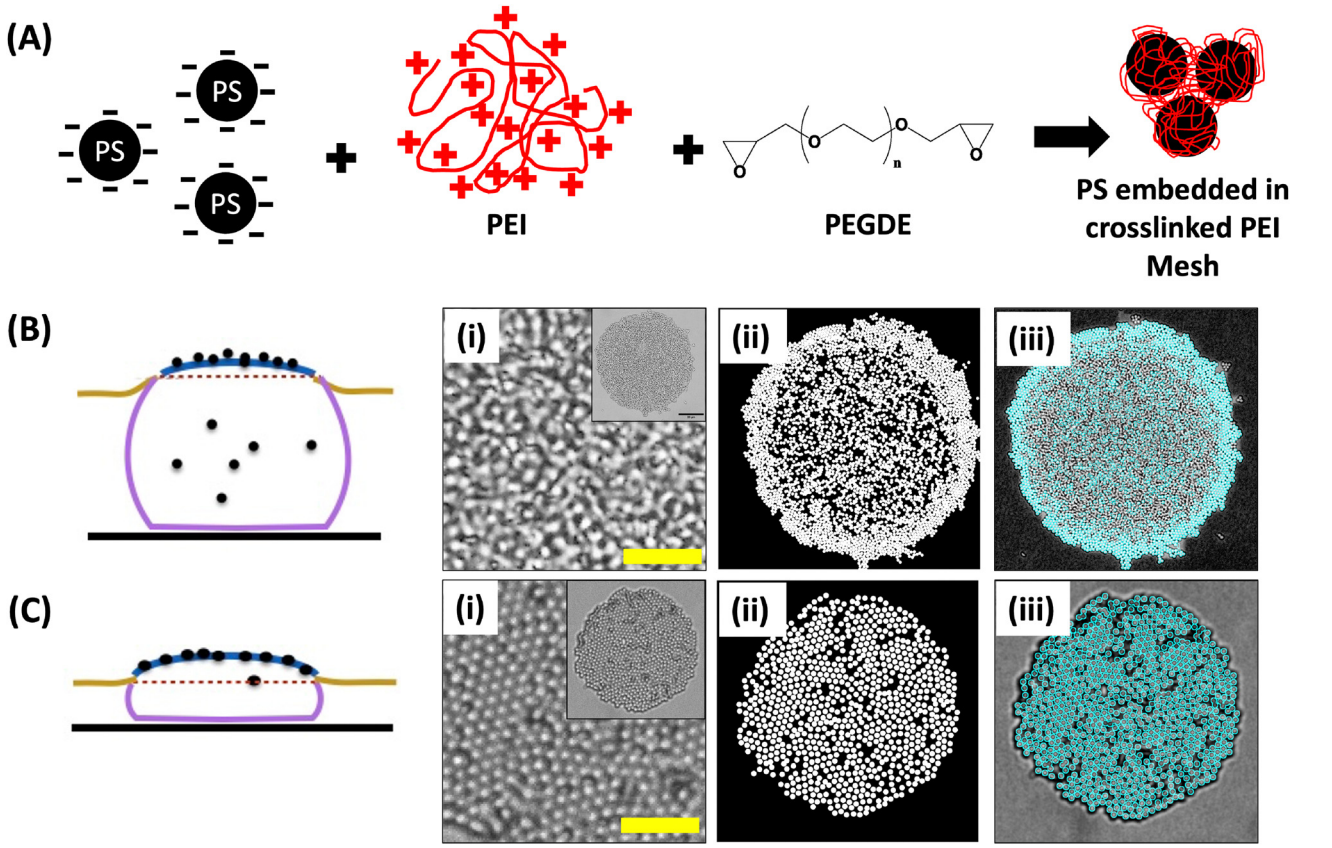

Fig. 1 (A) Preparation of PEI coated PS particles. Negatively charged PS particles are coated with positively charged PEI, and PEGDE is used to crosslink PEI which forms mesh around the particles. (B) Thick oil layers result in formation of non-monolayers as a significant number of particles still remain in bulk after interface becomes saturated as evaporation proceeds. (C) Thin oil layers lead to monolayers as most particles are adsorbed on to the surface before it becomes fully saturated on shrinking due to evaporation. In each case, the figures on the right show sample. Image-analysis steps for (B) non-monolayer and (C) monolayer sheets: (i) optical micrograph of the colloidal sheet, (ii) synthetically generated image using (x, y) coordinates of particles identified by image-analysis as belonging to a monolayer after removing non-monolayer regions, (iii) overlay of monolayer-particles coloured as cyan circles on original micrograph image. B(i) and C(i) show magnified images of the interior of the non-monolayer and monolayer assemblies, respectively; the insets show the complete assemblies, scale bar = 5 μm.

working solution was made by diluting 1.25 μL of this stock in 100 μL of Milli-Q water. The PS suspension was then gradually added to the PEI solution with intermittent vortexing to prevent aggregation. The mixture was stirred for 15 min to allow complete electrostatic adsorption of PEI onto the particle surfaces. Post-coating, the ζ-potential increased to 0.9 mV for PS, confirming surface saturation at near-neutral pH. A sessile 1 μL aqueous drop containing the desired number of colloidal particles as well as PEI and poly(ethylene glycol) diglycidyl ether (PEGDE) crosslinker was placed on a silicone oil-coated hydrophobic glass slide. The PEGDE to PEI weight ratio was kept constant at 0.01. The drops were dried at a constant temperature of 25 ± 3 °C and a relative humidity (RH) of 50 ± 5%. The evaporation process was monitored using an Olympus upright microscope (BX-53) equipped with 20×, and 100× objectives. The images were captured at a frame rate of 1 frame per second.

3.3 Estimation of monolayer fraction by image analysis

The optical micrograph of each sheet was converted into an 8-bit grayscale image. The threshold was then automatically determined using the iterative Isodata algorithm in ImageJ,[9] which calculates the threshold intensity as the mean of the average background and average object intensities. The algorithm iteratively updates the threshold value based on the intensity histogram until the threshold converges.

After converting optical micrographs to binary images, particles in monolayer regions appear as well-defined circles with diameters matching the known particle size. In contrast, non-monolayer regions exhibit arbitrary non-circular shapes and varying sizes, due to light refraction through multiple overlapping spherical particles. Image analysis was applied to the thresholded binary images to identify monolayer particles, defined as circular regions with an eccentricity greater than 0.8 and a diameter of 1 ± 0.1 μm. Panels C and B in Fig. 1 display representative images of monolayer and non-monolayer sheets. Each panel includes (i) the original optical micrograph, (ii) the binary image highlighting monolayer particles after removing non-monolayer regions, and (iii) an overlay of detected monolayer particles on the original micrograph. The monolayer fraction of a sheet is calculated as the ratio of the total

monolayer-particle area to the entire sheet area, as determined *via* image analysis. Sheets with a monolayer fraction of 85% or higher were classified as monolayers; otherwise, they were considered non-monolayers. In this work, we classify sheets as monolayers or non-monolayer based on image analysis. The term "non-monolayers" refers to any structure in which particles are not confined to a single layer at the interface; it does not imply a regular, stratified stacking of particles.

3.4 Hexatic order parameter characterisation

The centres of the monolayer-particles identified as described above were used to determine the hexatic order parameter for each particle. The hexatic order parameter ψ_i is calculated for any particle i as

$$\psi_i^6 = \frac{1}{N_i}\sum_{j=1}^{N_i} e^{i6\theta_{ij}}, \quad (1)$$

where N_i is the number of nearest neighbours of particle i, and θ_{ij} is the angle between the vector connecting particle i to its neighbour j and the x-axis. This order parameter evaluates how closely the arrangement of the nearest neighbours of that particle reflects a perfect six-fold symmetry. A value of 1 indicates perfect six-fold symmetry, while disordered regions have values close to zero. The centres of particles within a single colloidal layer were identified using the algorithm detailed in Section 3.3. Fig. 2 visualizes the distribution of the order parameter across a monolayer sheet containing approximately 5000 particles. Boundaries between highly-ordered domains with hexagonal close-packing of the particles and disordered regions are clearly visible.

To estimate the typical size of ordered regions, the spatial autocorrelation function of ψ was computed for each monolayer sheet as

$$C_{\psi^6}(r) = \frac{\overline{N_i^{-1}(r)\sum_{j(r)=1}^{N_i(r)}(\psi_i - \bar{\psi})(\psi_{j(r)} - \bar{\psi})}}{\overline{(\psi_i - \bar{\psi})^2}}. \quad (2)$$

Here, the overlines indicate averaging over all particles i in a given sheet and $\bar{\psi}$ is the average of the hexatic order parameter for the sheet; $N_i(r)$ is the number of neighbours of particle i located between r and $r + \delta$, and $j(r)$ is the j-th neighbour of particle i in that range. We set δ = 1 μm. The autocorrelation function defined above decays exponentially from 1 at r = 0 (Fig. 2B). In all our samples, the spatial autocorrelation function $C(r)$ was empirically observed to decay exponentially with distance. We use this functional form to fit the data and extract a characteristic length scale l_c, which serves as an estimate of the average size of ordered domains in each sheet. The correlation length l_c is determined as the characteristic length scale over which the autocorrelation decays exponentially, and provides a measure of the size of a typical ordered domain in a given sheet.

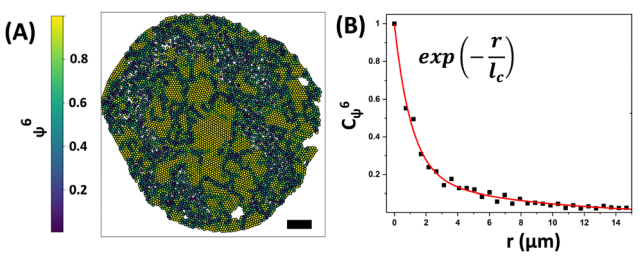

Fig. 2 (A) Typical hexatic order parameter (ψ^6) distribution in a monolayer sheet and (B) the corresponding spatial autocorrelation function (C_{ψ^6}) and the correlation length, l_c. Scale bar = 5 μm.

4 Results and discussion

4.1 Oil-layer thickness and monolayer formation

We conducted experiments following the procedure described previously.[8] Drops of aqueous suspensions of PEI-coated PS particles were deposited onto a hydrophobized glass substrate coated with silicone oil and then left to dry. The charge–neutral PEI-coated PS particles readily adsorbed at the water–air interface. After complete evaporation, the polymer was crosslinked, and the resulting sheets or structures were examined under a microscope. We investigated the effect of oil-layer thickness on suspensions containing different particle numbers. Fig. 3A presents representative micrographs of polymerized structures obtained at various oil-layer thicknesses and particle concentrations, while Fig. 3B shows a phase map depicting the conditions under which monolayers formed. Our results indicate a clear separation between monolayer and non-monolayer regimes, with the boundary following a systematic pattern.

Further evidence for the mechanism underlying the formation of monolayers comes from detailed time-lapse videos of the evaporating drops. Upon deposition, the drop rapidly penetrates the oil layer and assumes a spherical cap shape. Since the substrate is hydrophobic, the drop does not wet it, and a thin oil layer remains between the drop and the solid substrate. This configuration is consistent with previous studies on oleoplaning and slippery lubricant-infused surfaces, which demonstrate that an intercalating oil film just a few nanometers thick can persist between an aqueous droplet and a hydrophobic solid substrate.[8,10–14] The absence of contact line pinning and the smooth receding motion observed in our experiments are hallmark features of such lubricated systems. In cases where monolayers are formed (*e.g.* green box in Fig. 3A and panel C), as the water evaporates, most particles in the bulk suspension are first captured at the interface before they are pushed together by the shrinking area of the air–water interface. They form domains which are further assembled together into a sheet when the area shrinks sufficiently to be completely saturated by the particles. The process of monolayer formation does not involve the steady radial growth of a single domain. Instead, multiple domains nucleate independently across the curved interface, and these domains are further brought together to form a sheet when the area shrinks sufficiently to be completely saturated by the particles. Because these domains appear and evolve at different

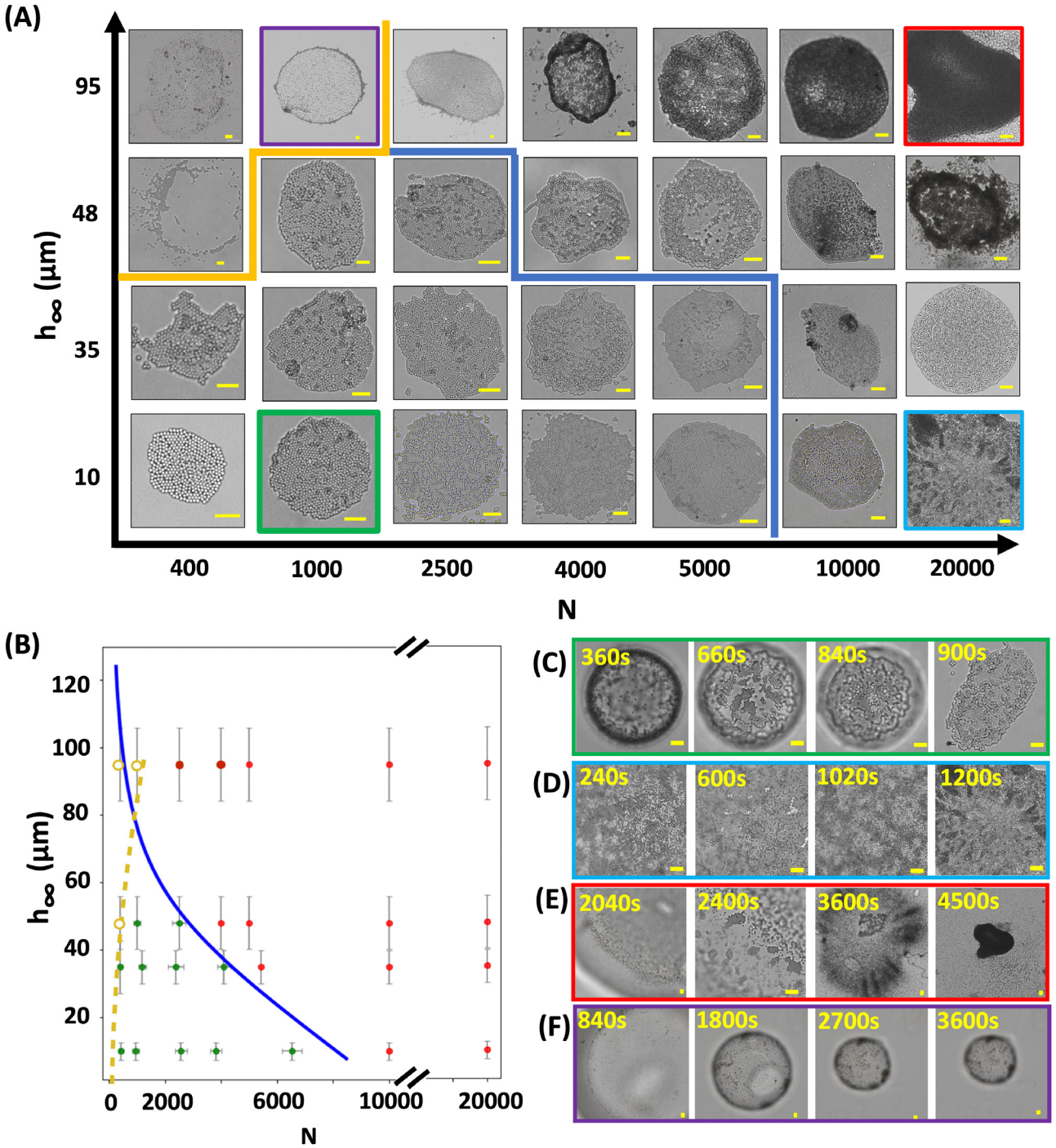

Fig. 3 (A) Optical micrographs of colloidal sheets formed at varying oil layer thicknesses h_∞ and particle numbers N for 1 μm-sized particles and an initial drop volume of 1 μL. The blue line separates monolayer sheets from contiguous but non-monolayer structures. The orange line marks the boundary between monolayer sheets and scattered, non-contiguous particle deposits that cannot be polymerized into a sheet. (B) Points in the (N,h_∞) space colour-coded according to whether a monolayer (green) was observed or not (red): error bars indicate the minimum and maximum observed values, and the blue line is the prediction obtained by solving eqn (7) in our model. Crosses indicate dispersed particles that could not be polymerized as single coherent structures. (C)–(F) Time-lapse images of sheet formation for the four cases in (A) as indicated by the coloured boxes; values indicate the time in seconds from the start of the evaporation. The scale bar on all microscopic images corresponds to 10 μm.

heights across the drop surface, they cannot all be captured simultaneously in a single focal plane, as observed, for instance, in Fig. 3C. Evaporation continues through gaps in this colloidal "skin" and finally a monolayer sheet is left behind. If the number of particles exceeds a critical threshold for a given oil-layer thickness (*e.g.* blue box in Fig. 3A and panel D), then as the drop evaporates, the interface becomes saturated with particles while there are still many particles

remaining in the interior of the drop. In this case, the final structure after evaporation is not a monolayer.

When the oil layer is large (*e.g.* purple and red boxes in Fig. 3A; panels E and F), the drop height falls below the oil layer height and the drop becomes submerged while a significant fraction of the particles still remain in the bulk. Evaporation then proceeds slowly *via* diffusion of water through the oil layer. Particles do not adsorb at the oil–water interface but remain suspended in the bulk. If the particle density is high, they form pellet-like aggregates as the volume decreases (*e.g.* red box in Fig. 3A; panel F), whereas at lower particle densities (*e.g.* purple box in Fig. 3A; panel E), the particles form scattered deposits that cannot be polymerized into a cohesive sheet.

4.2 Minimal model for monolayer formation

These observations suggest a model that qualitatively explains the role of oil-layer height in this process. We introduce the following simplifying assumptions. First, the droplet penetration time into the oil layer is much shorter than the overall evaporation time. The time scale for the water drop to submerge into the oil layer, driven by interfacial energy minimization, scales as $\tau \sim \mu h_\infty/\Delta\gamma$, where μ is the oil viscosity and $\Delta\gamma$ is the difference in interfacial tensions. For oil layers with $h_\infty <$ 100 μm, this gives $\tau < 10^{-2}$ s, which is negligible compared to the total evaporation time ($\sim 10^3$ s) in our experiments. Fig. 4A illustrates the initial shape of the droplet and the surrounding oil layers surface after deposition and penetration into the oil. The corresponding simplified geometry used in our model is shown in Fig. 4B. Experimental observations reveal a slight rise in oil height at the three-phase contact line, consistent with previous reports in the literature.[15–18] However, for simplicity, we neglect this effect in our model and assume that the oil-layer thickness, h_∞, remains unchanged by the presence of the droplet.

The thickness of the thin oil layer between the droplet and the substrate is negligibly small compared to both the initial droplet size and h_∞.[12] Furthermore, the effective contact angle at the pseudo-contact line on the substrate is expected to be slightly greater than 90°,[18,19] but for simplicity, we approximate it as 90° throughout the evaporation process until the air–water interface is fully covered by particles. Up to this point, the pseudo-contact line on the substrate remains mobile.

The initial Bond number, Bo = $\Delta\rho g R_0^2/\gamma$, for our droplets with an initial radius of R_0 = 0.5 mm, a water–oil density difference of $\Delta\rho$ = 30 kg m^{-3}, and an average surface tension coefficient γ = 0.040 N m^{-1} is of the order of 10^{-3}.[20]

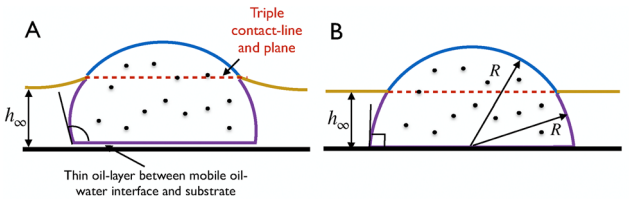

Fig. 4 (A) Geometry of the drop in the experiments. (B) Simplified geometry in the model.

As evaporation proceeds, the Bond number decreases further. As is well known, when the Bond number is small, the droplet shape is dictated entirely by surface tension. Consequently, the air–water and oil–water interfaces form sections of spherical caps. For a partially submerged drop, the curvatures of the air–water and oil–water interfaces, is determined firstly by the instantaneous volume of the drop and its contact angle with the substrate. The relative volumes above and below the air–oil–water contact line, as well as the air–water and oil–water interfacial tensions further modify these curvatures. However, since the surface tensions of the two interfaces (72 and 40 mN m^{-1}, respectively) are comparable in magnitude, as a first approximation, we neglect the differences between the curvatures and assume that the whole drop is a single spherical cap.

PEI-coated particles are charge–neutral, and dynamic interfacial tension measurements have previously confirmed the rapid adsorption of these particles at the water–air interface.[8] We therefore assume that the particles left behind by the evaporating water are immediately captured by the moving air–water interface. While the curvatures of these interfaces differ, we make the first-order assumption that they share the same radius of curvature. This assumption simplifies the droplet shape above the substrate to a hemispherical cap of radius R until the air–water interface reaches saturation. At any instant, the total droplet volume $V = 2\pi R^3/3$ and, from the geometry of spherical caps, the air–water interface area is

$$A_{AW} = 2\pi R^2\left(1 - \frac{h_\infty}{R}\right). \quad (3)$$

We now assume that the particles left behind by the evaporating water are immediately captured by the moving air–water interface. For particles that adsorb rapidly onto the interface, the adsorption flux is given by $c_i J_v$, where J_v is the volumetric evaporative flux of the liquid, and c_i is the particle concentration at the interface. Because this adsorption flux exactly matches the local particle loss due to evaporation, no concentration gradient develops at the interface. Given that the initial particle concentration within the drop is uniform, and no interfacial gradient emerges during evaporation, the concentration field within the drop remains uniform and constant throughout the process:

$$c = c_i = \frac{N_0}{V_0} = \frac{3N_0}{2\pi R_0^3},$$

where the subscript '0' refers to the initial state.

The crucial consequence of this uniformity is that the advective flux of particles, $\mathbf{u}\cdot\nabla c$, due to the internal capillary velocity field $\mathbf{u}$, is identically zero. Unlike in conventional coffee-ring systems—where particles are not captured by the interface and accumulate at the drop perimeter due to capillary flows—our system exhibits no such advective concentration buildup. This justifies our assumption that the velocity field plays no role in determining the spatial distribution of particles within the droplet.

Thus, in the case of rapidly adsorbing particles, When the drop radius shrinks to $R < R_0$, the number of particles adsorbed at the interface is given by:

$$N_a = c\frac{2\pi}{3}(R_0^3 - R^3) = N_0\left(\frac{R_0^3 - R^3}{R_0^3}\right). \quad (4)$$

At the point of interface saturation, the radius R_s satisfies:

$$N_0\left(\frac{R_0^3 - R^3}{R_0^3}\right)\chi a^2 = 2\pi R_s^2\left(1 - \frac{h_\infty}{R_s}\right), \quad (5)$$

where a is the particle radius, and χ is a factor dependent on the packing type. For instance, for hexagonal close packing in 2D, $\chi = 2\sqrt{3}$. To obtain monolayers, the interface must remain unsaturated even when only a single particle remains in the drop. We denote the radius at which adsorption is nearly complete and the number of unadsorbed particles in the drop decreases to one as R_c. This is related to N_0 and R_0 as:

$$N_0 = \left(\frac{R_0}{R_c}\right)^3. \quad (6)$$

For a given R_0 and h_∞, the maximum initial number of particles, $N_{0,max}$, that can assemble as a monolayer is determined by requiring that the surface becomes saturated exactly when only one unadsorbed particle remains. The drop radius at the point where the saturation and complete-adsorption conditions are simultaneously satisfied is denoted as $R_{s,c}$. Substituting $N_{0,max}$ in terms of $R_{s,c}$ from eqn (6) into eqn (5), we obtain:

$$2\pi R_{s,c}^5 - 2\pi h_\infty R_{s,c}^4 + \chi a^2 R_{s,c}^3 - \chi a^2 R_0^3 = 0. \quad (7)$$

With $\chi = 2\sqrt{3}$ and a = 1 μm, we find that, for the range of R_0 and h_∞ values in our experiments, a single real root for $R_{s,c}$ exists in the quintic equation above. The resulting values of $R_{s,c}$ were substituted into eqn (6) to obtain the blue curve for $N_{0,max}$ shown in Fig. 3(b).

Despite the simplifications, the model prediction closely matches the boundary of the monolayer regime observed in the experimental data. This agreement supports the argument that due to rapid adsorption at the interface, the velocity field within the droplet has minimal influence on the interfacial assembly of particles. This is in sharp contrast with conventional coffee-ring phenomena. In those cases, particles cannot adsorb into the interface as the liquid evaporates, leading to concentration gradients. The particles are then advected along the streamlines of the internal capillary flow and end up collecting at the points of maximum evaporative flux on the interface where the streamlines terminate.

At the oil–water interface, where the evaporative flux (due to water diffusing through the oil layer) J_v is much smaller than that at the air–water interface and the particle flux $c_i J_v \approx 0$; that is, there is no significant adsorption nor accumulation of particles. Consequently, the motion of the oil–water interface cannot drive particles toward the air–water interface and plays no direct role in particle assembly. Instead, a larger oil height h_∞ for the same drop radius R means that the available air–water interface area for particle assembly is relatively smaller as more of the overall surface is taken up by the passive oil–water interface. Further, the overall evaporation rate is also smaller.

The best conditions for monolayer formation occur with thin oil layers. For any given droplet volume, the range of particle numbers that yield monolayers is widest as $h_\infty \to 0$. To estimate the maximum achievable sheet size within the regime where our model applies, we consider the limiting case of vanishing oil layer thickness. Here, the relevant Bond number is Bo = $\rho g R_0^2/\gamma_{AW}$, with γ_{AW} the air–water interfacial tension. A Bond number of less than 10 corresponds to a droplet radius of approximately 5 mm, which, when substituted into our model, gives a particle number $N_0 \lesssim 10^5$ as the upper limit of monolayer sizes achievable in the capillary-dominated regime.

We note that a thin oil layer beneath the drop is essential: it prevents the polymerized sheet from adhering to the hydrophobic substrate during drying. Thus, although thinner oil layers are optimal for forming larger monolayers, the oil layer cannot be entirely eliminated in practice.

Cloaking of aqueous droplets by a thin oil film is a well-established phenomenon on lubricated surfaces, including systems similar to ours. Cloaking occurs when the spreading coefficient of the oil on water is positive:

$$S_{o/w} = \gamma_{wa} - \gamma_{wo} - \gamma_{oa}$$

where γ_{wa}, γ_{wo}, and γ_{oa} are the surface tensions of the water–air, water–oil, and oil–air interfaces, respectively. For silicone oils and water, this quantity is typically positive, indicating that the oil will spontaneously spread over the drop surface to minimize the interfacial energy. This has been confirmed in multiple studies of slippery lubricant-infused surfaces (SLIPS) and oleoplaning droplets[10–12] The resulting cloaking layer is extremely thin – typically in the range of 5–50 nm, depending on the oil viscosity, molecular structure, and interfacial tensions.[11] Its presence cannot be directly visualized using optical microscopy due to its nanometric thickness. In our experiments, the presence of such a cloaking film does not appear to hinder evaporation; water continues to diffuse through the thin oil layer into the air. Further, we experimentally observe that particles readily adsorb at the air–water interface, even in the presence of a cloaking layer. The model does not explicitly incorporate the evaporation flux; it further assumes rapid adsorption. Thus, the cloaking layer plays no role in the assumptions or predictions of our minimal model. The success in predicting the transition between monolayer and non-monolayer regimes suggests that finer-scale details such as cloaking are not dynamically relevant at the level of our analysis.

4.3 Particle ordering

Fig. 5(a) presents images of the spatial distribution of the hexatic order parameter in the monolayer sheets. The hexatic order parameter was obtained as described in Section 3.4. As shown in Fig. 5(b), for a given oil-layer thickness, the average

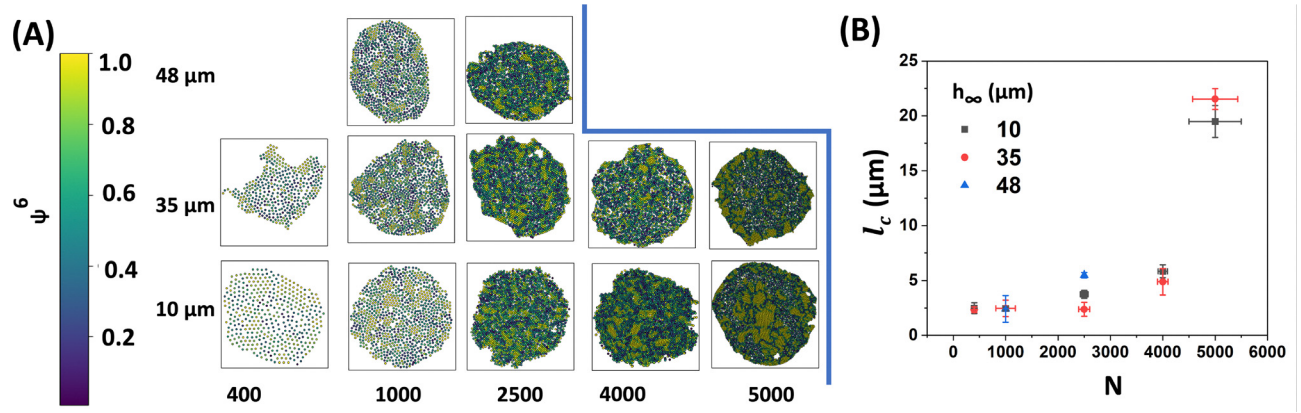

Fig. 5 (A) Spatial distribution of hexatic order parameter (Ψ_6) in monolayer sheets across particle concentrations (N) and oil layer thicknesses. (B) Variation of characteristic domain size (l_c) with number of particles (N) in the monolayer.

size of domains containing hexagonally close-packed particles increases with the number of particles, and consequently, with the sheet size. The domain size increases approximately linearly, doubling when the number of particles increases eightfold from around 500 to 4000. However, with a further 25% increase in particle number to 5000, the domain size exhibits an abrupt, nearly fourfold growth. This trend appears to be independent of the oil-layer thickness. However, the underlying mechanism behind this trend remains unclear. Note that while we focus on ordering in monolayer sheets here, a closer inspection of non-monolayer sheets formed at high particle concentrations (Fig. 3D and E) clearly shows crystalline ordering. Thus, colloidal particles form ordered assemblies when the dispersion concentration in the deposited drop exceeds a critical value.

Colloids at fluid interfaces represent model systems for investigating the evolution of order in two-dimensional systems.[21] Routes to glass formation in two-dimensional systems, comprising colloids with tunable interactions localized at interfaces have been reported.[22–24] Here, colloids have been shown to organize into clusters with local order, that frustrate the emergence of large scale crystalline ordering. Similar to the case of three-dimensional systems, the pathway to crystallization in two-dimensional colloidal systems is strongly determined by range and strength of interparticle interactions.[25] In a recent report, grazing incidence SAXS (GISAXS) was employed to investigate the crystallization of nanoparticles at a fluid interface.[26] It was suggested that electrostatic interactions resulted in a deformation of the fluid interface in the vicinity of particles, inducing a long-range attractive interaction that drove colloidal crystallization in two dimensions.

In our case, where monolayers form, particles are initially adsorbed at random locations on the air–water interface. This initial state can be considered a dilute 2D hard-sphere suspension. As evaporation proceeds, the shrinking interface leads to a progressive increase in the local particle density. Simultaneously, the rate at which particles are brought together by interface shrinkage can be characterized by a Peclet number. We have reported[8] that ordered colloidal rafts form above a critical dispersion concentration, and that as evaporation proceeds, these rafts come together to form a polydomain crystalline assembly. Capillary interactions appear to play an important role in generating attractive raft–raft interactions, especially during the later stages of evaporation. At lower dispersion concentrations, only disordered colloidal clusters are formed, that do not reorganize to form crystalline structures. It appears that only for specific combinations of the droplet dimensions and initial interfacial particle densities does the system, during evaporation, encounter an optimal interplay between increasing particle density and shrinkage-induced Peclet number that promotes crystallization. This scenario could explain why large crystalline domains emerge only under certain experimental conditions.

Although a detailed investigation of this phenomenon is beyond the scope of this work, a deeper understanding of the relationship between interfacial particle adsorption, evaporation dynamics, crystal nucleation, capillary attraction-induced aggregation and Péclet number could provide a framework for independently tuning both sheet size and crystalline domain size. In particular, adjusting parameters such as the oil-layer thickness h_∞, the number of adsorbed particles N, the initial droplet radius R_0, and the evaporation rate could offer greater control over monolayer formation and ordering.

5 Conclusions

Colloidal monolayers can be assembled at the air–water interface of evaporating sessile drops by coating colloidal particles with a suitable polymer, such as PEI, which promotes their adsorption at the interface. Crosslinking the polymer further stabilizes these monolayer sheets. In addition to particle coating, depositing the droplet on a hydrophobic surface with an oil layer is crucial. Monolayer formation depends on both particle concentration and oil layer thickness.

For a fixed oil layer thickness, increasing the number of particles in the droplet leads to continued accumulation until a saturation limit is reached, dictated by the packing fraction and maximum particle accommodation. A thicker oil layer reduces

the available air–water interface for evaporation, causing saturation to occur at lower particle concentrations. A simple theoretical model predicting the maximum achievable monolayer size based on the initial droplet volume, oil layer height, and particle size shows good agreement with experimental data. This agreement suggests that internal flow within the drop has minimal influence on particle adsorption at the interface.

Analysis of the hexatic order parameter in our monolayers reveals that crystalline domain sizes increase with particle concentration but remain unaffected by oil thickness. These findings suggest that the interplay between interfacial particle density and flow during interface shrinkage influences particle ordering and may govern the emergence of crystalline domains. Understanding this mechanism remains an open and intriguing problem in the field.

Our results also show that, for any given drop size, the widest range of monolayer sizes can be obtained by keeping the oil layer thin. This suggests that lubricant-impregnated surfaces (LIS), liquid-infused slippery surfaces (LISS), and slippery liquid-infused porous surfaces (LIPS)[15–17,19,27] could be ideal platforms for controlled synthesis of polymerized colloidal monolayers and for investigating tunable particle ordering in these monolayers.

Data availability

The data is presented in the manuscript. We will provide any additional clarification or details of analysis, upon reasonable request.

Conflicts of interest

There are no conflicts to declare.

Acknowledgements

ACYL acknowledges support from the Australian Research Council (FT180100594). SD acknowledges the IITB-Monash Academy for a PhD fellowship. The authors acknowledge the use of the instruments and scientific and technical assistance of Dr Xi-Ya Fang at the Monash Centre for Electron Microscopy, Monash University, a Microscopy Australia (ROR: 042mm0k03) facility supported by NCRIS. The authors are also grateful to Prof. Chris MacNiell (Monash University, Materials Science and Engineering) and the Monash Centre for Electron Microscopy (MCEM) for access to their experimental facilities.

Notes and references

1 H. Li, Y. Duan, Z. Shao, G. Zhang, H. Li, Y. Huang and Z. Yin, *Adv. Mater. Technol.*, 2020, **5**, 2000401.
2 D. A. Chalkias, A. Mourtzikou, G. Katsagounos, A. Karavioti, A. N. Kalarakis and E. Stathatos, *Sol. RRL*, 2022, **6**, 2200196.
3 M. B. Bigdeli and P. A. Tsai, *Langmuir*, 2020, **36**, 4835–4841.
4 F. Fan and K. J. Stebe, *Langmuir*, 2004, **20**, 3062–3067.
5 R. D. Deegan, O. Bakajin, T. F. Dupont, G. Huber, S. R. Nagel and T. A. Witten, *Nature*, 1997, **389**, 827–829.
6 P. J. Yunker, T. Still, M. A. Lohr and A. Yodh, *Nature*, 2011, **476**, 308–311.
7 M. Rey, J. Walter, J. Harrer, C. M. Perez, S. Chiera, S. Nair, M. Ickler, A. Fuchs, M. Michaud and M. J. Uttinger, *et al.*, *Nat. Commun.*, 2022, **13**, 2840.
8 S. V. Daware, R. Mondal, M. Kothari, A. Chowdhury, A. C. Liu, R. Prabhakar and G. Kumaraswamy, *Langmuir*, 2024, **40**, 23198–23208.
9 T. J. Collins, *Biotechniques*, 2007, **43**, S25–S30.
10 J. D. Smith, R. Dhiman, S. Anand, E. Reza-Garduno, R. E. Cohen, G. H. McKinley and K. K. Varanasi, *Soft Matter*, 2013, **9**, 1772–1780.
11 F. Schellenberger, J. Xie, N. Encinas, A. Hardy, M. Klapper, P. Papadopoulos, H.-J. Butt and D. Vollmer, *Soft Matter*, 2015, **11**, 7617–7626.
12 D. Daniel, J. V. Timonen, R. Li, S. J. Velling and J. Aizenberg, *Nat. Phys.*, 2017, **13**, 1020–1025.
13 A. Gao, J. Liu, L. Ye, C. Schönecker, M. Kappl, H.-J. Butt and W. Steffen, *Langmuir*, 2019, **35**, 14042–14048.
14 B. Bhatt, S. Gupta, M. Sharma and K. Khare, *J. Colloid Interface Sci.*, 2022, **607**, 530–537.
15 M. Tress, S. Karpitschka, P. Papadopoulos, J. H. Snoeijer, D. Vollmer and H.-J. Butt, *Soft Matter*, 2017, **13**, 3760–3767.
16 M. R. Gunjan, A. Kumar and R. Raj, *Langmuir*, 2020, **36**, 2974–2983.
17 M. Sharma, S. S. Mondal, P. K. Roy and K. Khare, *J. Colloid Interface Sci.*, 2020, **569**, 244–253.
18 M. Sharma, B. Bhatt, S. Gupta, R. Pant and K. Khare, *Bull. Mater. Sci.*, 2020, **43**, 1–7.
19 S. Gupta, B. Bhatt, M. Sharma and K. Khare, *Soft Matter*, 2023, **19**, 1164–1173.
20 A. W. Adamson and A. P. Gast, *et al.*, *Physical chemistry of surfaces*, Interscience publishers, New York, 1967, vol. 150.
21 O. Marnette, E. Perez, F. Pincet and G. Bryant, *Colloids Surf., A*, 2009, **346**, 208–212.
22 F. Ebert, P. Keim and G. Maret, *Eur. Phys. J. E:Soft Matter Biol. Phys.*, 2008, **26**, 161–168.
23 F. Ebert, G. Maret and P. Keim, *Eur. Phys. J. E:Soft Matter Biol. Phys.*, 2009, **29**, 311–318.
24 E. Tamborini, C. P. Royall and P. Cicuta, *J. Phys.:Condens. Matter*, 2015, **27**, 194124.
25 B. Li, X. Xiao, S. Wang, W. Wen and Z. Wang, *Phys. Rev. X*, 2019, **9**, 031032.
26 L. Wu, X. Wang, G. Wang and G. Chen, *Nat. Commun.*, 2018, **9**, 1335.
27 S. Sahoo and R. Mukherjee, *arXiv*, 2023, preprint, arXiv:2311.14406, **https://arxiv.org/abs/2311.14406**.